

RESEARCH

Open Access



DNA methylation memory of pancreatic acinar-ductal metaplasia transition state altering Kras-downstream PI3K and Rho GTPase signaling in the absence of Kras mutation

Emily K.W. Lo^{1,2,3,4}, Adrian Idrizi^{2,4}, Rakel Tryggvadottir^{2,4}, Weiqiang Zhou⁵, Wenpin Hou⁵, Hongkai Ji⁵, Patrick Cahan^{1,3*} and Andrew P. Feinberg^{1,2,4*}

Abstract

Background A critical area of recent cancer research is the emergence of transition states between normal and cancer that exhibit increased cell plasticity which underlies tumor cell heterogeneity. Pancreatic ductal adenocarcinoma (PDAC) can arise from the combination of a transition state termed acinar-to-ductal metaplasia (ADM) and a gain-of-function mutation in the proto-oncogene *KRAS*. During ADM, digestive enzyme-producing acinar cells acquire a transient ductal epithelium-like phenotype while maintaining their geographical acinar organization. One route of ADM initiation is the overexpression of the *Krüppel-like factor 4* gene (*KLF4*) in the absence of oncogenic driver mutations. Here, we asked to what extent cells acquire and retain an epigenetic memory of the ADM transition state in the absence of oncogene mutation.

Methods We profiled the DNA methylome and transcriptome of *KLF4*-induced ADM in transgenic mice at various timepoints during and after recovery from ADM. We validated the identified DNA methylation and transcriptomic signatures in the widely used caerulein model of inducible pancreatitis.

Results We identified differential DNA methylation at Kras-downstream *PI3K* and *Rho/Rac/Cdc42 GTPase* pathway genes during ADM, as well as a corresponding gene expression increase in these pathways. Importantly, differential methylation persisted after gene expression returned to normal. Caerulein exposure, which induces widespread digestive system changes in addition to ADM, showed similar changes in DNA methylation in ADM cells. Regions of differential methylation were enriched for motifs of KLF and AP-1 family transcription factors, as were those of human pancreatic intraepithelial neoplasia (PanIN) samples, demonstrating the relevance of this epigenetic transition state memory in human carcinogenesis. Finally, single-cell spatial transcriptomics revealed that these ADM transition cells were enriched for PI3K pathway and AP1 family members.

Conclusions Our comprehensive study of DNA methylation in the acinar-ductal metaplasia transition state links epigenetic memory to cancer-related cell plasticity even in the absence of oncogenic mutation.

Keywords Pancreatic cancer, DNA methylation, Epigenetic memory

*Correspondence:

Patrick Cahan
patrick.cahan@jhmi.edu
Andrew P. Feinberg
afeinberg@jhu.edu

Full list of author information is available at the end of the article



© The Author(s) 2025. **Open Access** This article is licensed under a Creative Commons Attribution 4.0 International License, which permits use, sharing, adaptation, distribution and reproduction in any medium or format, as long as you give appropriate credit to the original author(s) and the source, provide a link to the Creative Commons licence, and indicate if changes were made. The images or other third party material in this article are included in the article's Creative Commons licence, unless indicated otherwise in a credit line to the material. If material is not included in the article's Creative Commons licence and your intended use is not permitted by statutory regulation or exceeds the permitted use, you will need to obtain permission directly from the copyright holder. To view a copy of this licence, visit <http://creativecommons.org/licenses/by/4.0/>.

Background

Pancreatitis is a major risk factor for the development of pancreatic ductal adenocarcinoma (PDAC), one of the deadliest malignancies in the USA [1, 2]. PDAC develops in the exocrine compartment of the pancreas, which comprises acini, the cells responsible for synthesizing digestive enzymes, and ductal epithelial cells which transport digestive juices to the small intestine. A characteristic feature of pancreatitis is a transition state called acinar-to-ductal metaplasia (ADM), in which acinar cells acquire a transient ductal-like phenotype. ADM supports tissue regeneration and protection in response to injury and is normally followed by reversion to a normal acinar phenotype [3].

The combination of ADM with an oncogenic mutation in the *KRAS* gene, the most commonly mutated gene in pancreatic cancer [4, 5], drives the formation of neoplastic precursor lesions [3]. Although ADM alone is insufficient to drive the formation of neoplastic lesions, recent cancer research has placed more emphasis on the investigation of such cellular transition states prior to driver gene mutation and how they may underlie or enable cancer initiation [6, 7]. For example, the links between esophageal adenocarcinoma and Barrett's esophagus and between gastric adenocarcinoma and gastric metaplasia [8] highlight the key role that cell fate transition states play in cancer development. The epigenetic basis of these transition states is of particular interest, as the epigenome facilitates cell identity and memory [9–12]. Furthermore, the epigenome is also of particular interest in pancreatic cancer, as epigenetic changes have already been shown to facilitate the primary-to-metastasis transition without the acquisition of additional driver mutations [13–15].

The role of the epigenome remains elusive in establishing and maintaining the ADM transition state. More specifically, DNA methylation, which confers stable, long-term epigenetic memory via maintenance across cell divisions [10, 16], has not been comprehensively profiled in ADM. Here, we investigate the DNA methylation landscape and corresponding transcriptional landscape of the mutation-free ADM transition state and the subsequent reversion to a normal acinar phenotype. We ask to what extent cells retain a memory of the ADM transition state via DNA methylation, examine potential regulators of altered DNA methylation during ADM, and investigate the relationship of the ADM transition state to human pancreatic cancer precursor lesions. These findings may inform the mechanisms not only of heritable epigenetic memory of transition states and inflammation, but also of how epigenetic alterations presage or even elicit genetic mutations in cancer.

Methods

Animal models and cohorts

All animal procedures were performed in accordance with Johns Hopkins University Animal Care and Use Committee-approved protocols MO18M24 and MO21M20. *Ptf1a-rtTA*, *TRE-KLF4* (AK) mice were generated by crossing strain B6.129S6(SJL)-*Ptf1atm*^{3.1(rtTA)^{Mgn}}/Mmjax (Jackson Laboratories, cat. #036492-JAX) with strain FVB.Cg-Tg(tetO-KLF4)32831Rup/Mmjax (Jackson Laboratories, cat. #036730-JAX). Mice were genotyped using JAX-specified primers and protocols. ADM was induced by administering 12.5 mg/kg doxycycline intraperitoneally once every 24 h for 2 days. For caerulein-induced pancreatitis, C57BL/6 J wild-type mice (Jackson Laboratories, cat. #000664) were administered 0.625 mg/kg caerulein (Millipore Sigma, cat. #C9026) or saline sham negative control intraperitoneally 4× daily for 2 days. All animals were between 6 and 28 weeks of age. All animals and related metadata, including sex, treatment, timepoint, body weight, and pancreas weight, are described in Additional File 1: Table S1. Pancreata were extracted and processed from at least $n=2$ animals per condition and timepoint combination, as described in the following sections. Prior to pancreatic extraction, animals were euthanized according to AVMA guidelines via CO₂ asphyxiation at a displacement rate of 30–70% for 2–4 min, followed by 3–6 minutes of continued exposure, and finally cervical dislocation to verify death.

Pancreatic extraction and processing

Following euthanasia, pancreata were immediately harvested. A 2–4-cm incision was made in the abdominal skin along the midline and then into the abdomen. Pancreata were exteriorized and removed using a combination of blunt and sharp dissection. The tail of each pancreas was immediately flash frozen in liquid nitrogen for 5 min, then transferred to -80°C for long-term storage. The head of each pancreas was placed in 10% neutral-buffered formalin for fixation for 24 h, then transferred to 70% ethanol. Tissue was then dehydrated in a graded ethanol and xylene series, then embedded in paraffin. Paraffin tissue blocks were stored long term at 4°C .

Histology

For hematoxylin and eosin (H&E) staining, formalin-fixed, paraffin-embedded (FFPE) tissue was sectioned at 4 μm thick onto charged slides (Fisherbrand #12–550–15). Tissue sections were rehydrated in xylenes and a graded ethanol series. Slides were incubated in Gill's No. 2 hematoxylin for 1 min, then blued in tap water for 5 min. Slides were then incubated in alcoholic eosin Y

solution for 1 min, then dehydrated in a graded ethanol and xylene series. Coverslips were mounted using Histo-mount mounting solution (ThermoFisher, cat. #008030).

qRT-PCR

RNA was extracted from frozen pancreatic tissue using RNeasy Mini Kit (QIAGEN, # 74,104) according to the manufacturer's instructions. RNA was reverse transcribed to cDNA according to the manufacturer's instructions for SuperScript IV Reverse Transcriptase (ThermoFisher #18090010). Assuming an 80% reverse transcription efficiency, qPCR was performed according to the manufacturer's instructions for iTaq Universal SYBR Green Supermix (BioRad #1725121). PCR and fluorescence quantification were performed using a BioRad CFX 384 Real-Time PCR System. Primer sequences for qPCR are available in Additional File 2: Table S2.

Laser capture microdissection (LCM)

Fresh frozen tissue samples were cryo-sectioned at 10 μ m thick onto PEN membrane slides and stored at -20°C . Immediately prior to LCM, slides were fixed briefly in 70% ethanol, then stained with hematoxylin and eosin. LCM for the appropriate targeted cell type was performed using Zeiss PALM Microbeam on $\times 10$ or $\times 20$ magnification. The number of pooled cuts per cell type needed to reach a desired input of at least 20 ng DNA for WGBS varied for each sample. Genomic DNA was extracted using QIAamp DNA Micro Kit (Qiagen cat. #56304) according to the manufacturer's instructions for the "Isolation of Genomic DNA from Laser-Microdissected Tissues" protocol, with carrier RNA inclusion. To increase final DNA yield, samples were eluted twice, using the eluate from the first elution for the second, and incubating for 5 min each before centrifugation.

Whole-genome bisulfite sequencing (WGBS)

Genomic DNA samples were quantified by Qubit dsDNA HS assay (ThermoFisher Scientific, cat. #Q32851). 1% unmethylated Lambda DNA (Promega cat. #D1521) was spiked into genomic DNA to monitor bisulfite conversion efficiency. xGen Methyl-Seq DNA Library Prep Kit (IDT, cat. #10009860) was used for WGBS library preparation. Genomic DNA (19–50 ng) was fragmented to a target peak of 300–400 bp using the Covaris S2 Focused-ultrasonicator in a 50 μ l volume according to the manufacturer's instructions. The fragmented genomic DNA was subjected to bisulfite conversion using the EZ DNA Methylation-Gold Kit (Zymo Research, cat. #D5005) following the manufacturer's instructions. Methyl-seq libraries were generated according to the manufacturer's instructions, and the resulting libraries were amplified for 7 PCR cycles using unique dual indexing primers (Swift

Bioscience, cat. #X9096-PLATE). The resulting WGBS libraries were evaluated on a 2100 Bioanalyzer using the Agilent High-Sensitivity DNA Kit (Agilent Technologies, cat. #5067–4626) and quantified via qPCR using the KAPA Library Quantification Kit (KAPA Biosystems, cat. #KK4824). WGBS libraries were sequenced on an Illumina NovaSeq 6000 system at a 2×150 bp read length with a 5% spike-in of PhiX control library.

WGBS variant calling

Bisulfite-aware variant calling was performed as previously described [17]. Briefly, python software Revelio [18] was used to mask base positions potentially altered due to bisulfite treatment. Variant detector freebayes [19] was used on Revelio-masked bam files to identify mutations in the coding sequences of the most commonly mutated genes in PDAC [5, 20]. VCF (Variant Call Format) files outputted by freebayes were then converted into MAF (Mutation Annotation Format) files via *vcf2maf*. Finally, the Bioconductor package *maftools* [21] was used to analyze the type and distribution of the given mutations, with a read coverage threshold of 30 and a variant detection threshold of 3 reads.

WGBS analysis

Adapter sequences were computationally trimmed with Trim Galore (<https://github.com/FelixKrueger/TrimGalore>), with 10 additional bp trimmed from the 3' end of R1 and 10 bp from the 5' end of R2 to account for the low complexity polynucleotide tail added by the Adaptase enzyme. Bisulfite-aware alignment of the trimmed reads to the mm10 genome was performed using Bismark [22] with default parameters. Samtools was used to merge individual bam files corresponding to fastq file pairs and to name-sort the merged bam file. Bismark was then used to deduplicate merged, name-sorted bam files, then extract CpG methylation information. Bisulfite conversion rate was determined by alignment of trimmed reads to the lambda genome using Bismark with default parameters. Bisulfite conversion rate was at least 99.2% for all samples, with an average of 99.34% among all samples.

The Bioconductor package *bsseq* [23] was used for integrating independent CpG_report files from Bismark's *methylation_extractor*. CpG methylation values for each sample were smoothed with the *BSsmooth* function using default parameters. Principal component analysis (PCA) was performed on smoothed methylation values generated by *bsseq* using the *prcomp* function from the R stats package, with parameters *scale=TRUE* and *center=TRUE*.

For differential methylation analysis, smoothed CpG methylation values from autosomes were coverage-filtered with a cutoff of 2X for each biological replicate.

DMR-finding was limited to autosomes to help mitigate potential bias introduced by sex. For pairwise comparisons, BSmooth.tstat was used to compute *t*-statistics between groups, with $k=21$ and local.correct=TRUE. Significant DMRs were identified using *t*-statistic quantile cutoffs of 0.05 and 0.95, and these DMRs were filtered using a CpG number cutoff of $n \geq 5$ and a mean methylation difference cutoff of 10%. If two CpGs within a DMR were more than 300 bp apart, the DMR was split into two separate DMRs.

Fisher's exact gene set enrichment analysis (Fisher's GSEA) was performed using web program Enrichr [24], a gene set overrepresentation analysis software based on Fisher's exact test. First, genes overlapping DMRs found by bsseq were identified. Genomic annotations for mm10 genes were generated via Bioconductor package annotatr [25], then DMR-gene intersections were identified using the findOverlaps function from Bioconductor package GenomicRanges [26]. Gene lists were input into Enrichr, and output tables for Reactome 2022 enrichment were visualized using R package ggplot2 [27].

Visium FFPE spatial transcriptomics (ST)

Whole-transcriptome ST was performed using Visium Spatial Gene Expression Reagent Kits for FFPE (10X Genomics #1000185, #1000362, and #1000366). Mouse probe set Visium_Mouse_Transcriptome_Probe_Set_v1.0_mm10-2020-A was used. Prior to library preparation, the DV200 quality metric of RNA from FFPE pancreas tissue was first verified using RNA 6000 Nano Kit (Agilent #5067–1511) according to the manufacturer's instructions. All pancreas sections used as input for Visium ST had a DV200 of $\geq 57\%$, with most samples $\geq 70\%$. Library preparation was performed according to the manufacturer's instructions (CG000407, Rev. A), with the following custom parameters: (1) each H&E-stained section was imaged in 12 parts on a Nikon Eclipse Ti Research Photomicroscope at $\times 4$ magnification, then images were stitched post-capture using ImageJ; (2) 0.5 μ L RNase Block (Agilent #300,151) was added per sample (e.g., 2.2 μ L for 4X + 10%) at pre-hybridization (Step 1.1.a) and probe hybridization (Step 1.1.g); and (3) PCR cycle number (Step 4.2.d) ranged from 14 to 17 depending on the Cq value from Step 4.1.e. Sample Index PCR (Step 4.2.a) for each sample was performed with a unique index well from Dual Index Plate TS Set A (10X Genomics #3000511). The 20 FFPE Visium libraries were sequenced on one lane of an S4 flowcell on an Illumina NovaSeq 6000 system at a 2×150 bp read length. Libraries were loaded onto the flowcell at a ratio to achieve at least 25,000 reads per spatial spot covered by tissue.

MERFISH

MERFISH was performed using the Vizgen MERSCOPE platform. MERSCOPE sample verification (Vizgen #10400008) was performed on pancreas FFPE tissue to verify RNA and tissue quality according to the manufacturer's instructions (91600004, Rev D). MERSCOPE gene imaging (Vizgen #10400006) was performed on AK D2, D4, D7, and normal acinar samples according to the manufacturer's instructions (91600112, Rev B), with the following sample-specific parameters: (1) cell boundary stain 3 (Vizgen #10400009) was used, (2) non-resistant FFPE tissue clearing protocol was performed, and (3) probe hybridization was performed for 48 h. Custom 500-gene panel (Vizgen #10400003, Panel ID 6c74b9d8-2814-4e73-97dd-435ea4062659, Serial Number CP1069) is detailed in Additional File 3: Table S3.

Analysis of Visium data

Visium data was preprocessed using spaceranger (v 1.3.0) against 10X Genomics-provided mm10 reference transcriptome build refdata-gex-mm10-2020-A to generate gene-by-spot expression matrices. If necessary, manual image alignment was performed using the 10X Loupe Browser (v 5.1.0). R package Seurat [28] was used to log-normalize, integrate, and perform Leiden clustering on spot expression profiles.

Deconvolution tool RCTD [29] was used to assign cell identity proportions to Visium spot expression data. RCTD was trained on a combination of manually annotated pure Visium spots and publicly available single-cell datasets. Manual annotation of spots with pure compositions of acini, adipose tissue, ADM, duct, or endocrine cells was performed using the 10X Loupe Browser. For supporting cell types including B cells, endothelial cells, fibroblasts, macrophages, pericytes, and T cells, five publicly available pancreatic single-cell datasets (Additional File 4: Table S4) were normalized by SCTransform and integrated with reciprocal PCA using Seurat. To create training profiles that would be comparable to manually annotated spots in terms of order of magnitude of counts, pseudobulk profiles were created by summing the counts by gene of 10 randomly selected cells of the same type. RCTD was performed using the following parameters: gene_cutoff=0.000125, fc_cutoff=0.5, UMI_min=100, UMI_max=2E+07, UMI_min_sigma=300, CELL_MIN_INSTANCE=25, CONFIDENCE_THRESHOLD=10, doublet_mode="full". Following RCTD deconvolution, only exocrine spots in the top 90th percentile of a given cell type proportion with no other greater cell type proportion were used for downstream differential expression analysis with Seurat.

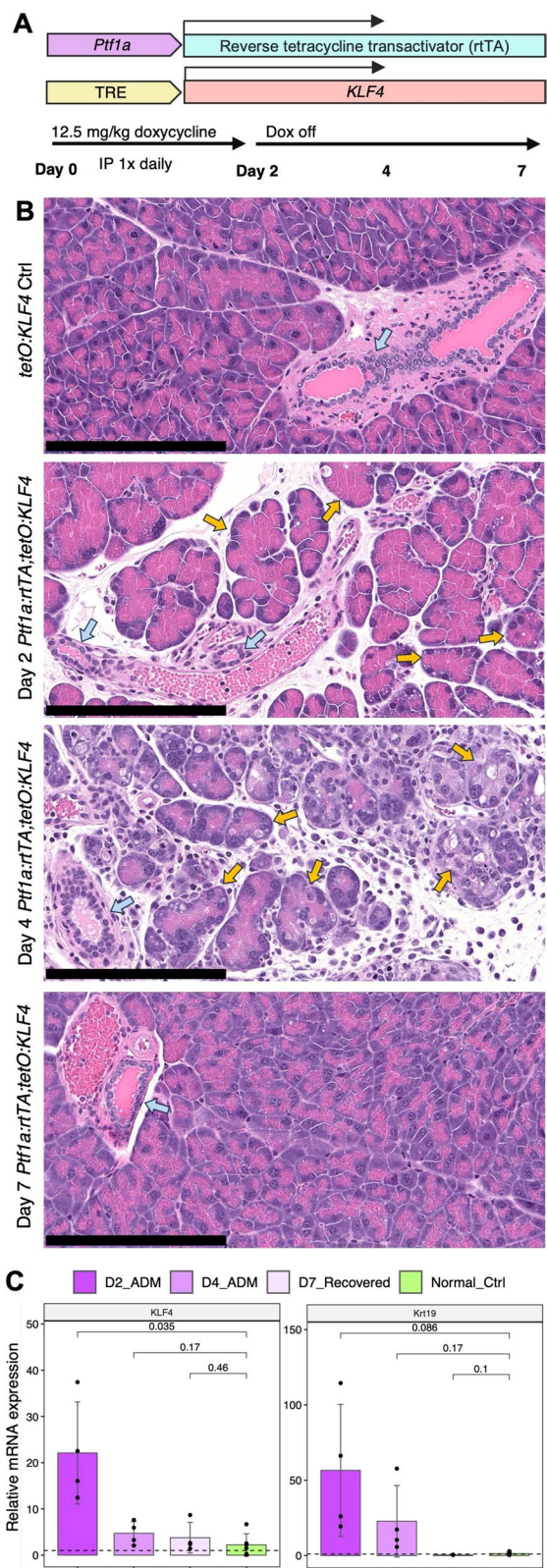


Fig. 1 Genetically engineered mouse model of inducible acinar-specific KLF4 expression for induction of acinar-ductal metaplasia (ADM). **A** Schematic of *Ptfla-rtTA*, *TRE-KLF4* (AK) model and doxycycline administration schedule. TRE: Tet-response element. IP: Intraperitoneal. **B** Representative hematoxylin and eosin staining of normal control, and day 2, day 4, and day 7 pancreata as in administration schedule in **A**. Blue arrows: normal ducts. Yellow arrows: ADM. Scale bar: 200 μ m. **C** Relative mRNA expression of murine *Krt19* and human *KLF4* as quantified by qRT-PCR. $n = 2$ mice. p -values: two-sided t -test. Error bars: SD

Analysis of MERFISH data

Raw MERSCOPE data was preprocessed using the MERSCOPE Visualizer. Processed Vizgen datasets were log-normalized and integrated with reciprocal PCA using Seurat. Cell type co-expression analysis was performed using a list of canonical marker genes for each cell type (Additional File 3: Table S3). Genes from the target gene panel related to PI3K and AP-1 were annotated based on KEGG, GO BP, and Reactome gene sets from MSigDB [30]. For each cell, to normalize for cell–cell variability in MERSCOPE transcript detection, the proportion of unique gene pair combinations of x number of markers of cell type A and y number of markers of cell type B out of the total possible unique gene pairs in a cell was calculated. To normalize for random expectation, for each cell we then calculated the co-expression probability of x and y randomly selected markers without replacement. We reported the log2 fold change (signal/random) for each cell in each sample per A-B cell type pair.

Transcription factor motif analysis

Transcription factor motif analysis at DMRs was performed using software package Homer [31]. For each differential methylation comparison, a.txt file specifying the genomic coordinates of each DMR, plus 50 bp of buffer on each side, was generated in R. Homer’s find-MotifsGenome.pl program was run on each.txt file with mm10 genome and -size 200.

Results

ADM differentially methylated regions are enriched

in *Kras*-downstream PI3K and Rho GTPase pathway genes
We first sought to generate a mouse model that targeted ADM induction to acinar cells in the absence of oncogenic driver mutations. To this end, we bred *Ptfla-rtTA*; *TRE-KLF4* (AK) mice, which enabled inducible, acinar-specific overexpression of human *Krüppel-like factor 4* (*KLF4*) (Fig. 1A). *Klf4* is a known player in injury and inflammation [32, 33] and has been found to be necessary and sufficient for ADM in mouse models of pancreatitis

[34]. A 2-day administration of doxycycline in AK mice induced key histological features of acute pancreatitis, including prominent structural changes and vacuolation in acinar cells by day 2 (D2) and increased stromal and immune cell presence by day 4 (D4), followed by recovery to a normal acinar phenotype by day 7 (D7), while normal ductal cells were unchanged during the same time course (Fig. 1B). We also examined changes in pancreas weight over the time course. We observed that AK animals exhibited a decreased pancreas weight as a percent of total bodyweight, which was corroborated by animal weights in a widely used model of pancreatitis induction by caerulein (Additional File 1: Table S1, Additional File 5: Fig. S1A). Nevertheless, the normal histology of pancreata at D7 and the high expression of *KLF4* and ADM marker gene *Krt19* in D2 relative to normal pancreata quantified by qPCR validated not only temporally appropriate induction of *KLF4* but also corresponding upregulation of and recovery from an ADM-associated phenotype (Fig. 1B,C). Taken together, these results demonstrate that targeted overexpression of *KLF4* to acinar cells is sufficient to reproduce the physiological characteristics of ADM, and that ADM can be induced in a cell-intrinsic manner.

To profile the DNA methylome of individual exocrine cell types during ADM, we performed whole-genome bisulfite sequencing (WGBS) on histologically pure tissue fragments of acini, ADM lesions, and ducts isolated using laser-capture microdissection (LCM) at days 2, 4, and 7 (Additional File 6: Table S5, Additional File 5: Fig. S1B) [35]. Hundreds of micro-dissected regions were pooled per animal to achieve sufficient DNA yield and to provide robustness against variation that might result from profiling individual cuts. To validate the lack of canonical PDAC mutations in the AK model, we performed bisulfite-aware variant calling on all AK WGBS samples. We did not find any mutations in the top 4 genes mutated in PDAC (*Kras*, *Tp53*, *Smad4*, or *Cdkn2a*) [5, 20] in any sample (Additional File 7: Table S6). Additionally, almost all genes with variants in the AK mice had an equivalent variant in the littermate control mice, suggesting that these are variants associated with the mouse strain and not associated with or induced by ADM.

Principal component analysis (PCA) on genome-wide CpG methylation grouped normal acini and ADM lesions separately, with recovered acini forming an intermediate group (Fig. 2A), demonstrating a detectable global difference in DNA methylation based on ADM status. When ducts were included, PCA grouped ducts separately from all other cell types at principal components 1 and 2 (Additional File 5: Fig. S1B), consistent with methylation studies in humans [17]. However, principal components 3 and 2 still demonstrated meaningful separation

of normal acini and ADM lesions and an intermediate status of recovered acini (Additional File 5: Fig. S1C). Both genome-wide and at promoters specifically, there was no significant difference in CpG methylation level among normal acini, ADM lesions, and recovered acini, and methylation level was greater in ducts relative to the acinar-derived cell types (Additional File 5: Fig. S1C). However, examining DNA methylation globally often obscures important gene-level changes; thus, we next sought to identify specific genes with altered methylation during ADM.

We first performed mean-based differentially methylated region- (DMR-) finding to compare D2 and D4 ADM lesions to normal acinar controls in the AK model. Meta-region analysis of all samples at ADM vs acinar DMRs specifically demonstrated that D7 recovered samples, on average, had an intermediate methylation level between ADM and acinar samples, regardless of DMR directionality (Fig. 2B, Additional File 8: Fig. S2A). Analysis of genomic features overlapping these DMRs revealed an enrichment of DMRs over promoters, enhancers, and gene bodies, as well as CpG shores [36] and shelves, relative to negative control randomly selected genomic regions (Additional File 8: Fig. S2B). Furthermore, Fisher's exact gene set overrepresentation analysis (Fisher's GSEA) of genes overlapping ADM vs acinar DMRs at both D2 and D4 (Additional File 11: Table S7) revealed an enrichment of pancreatic acinar-related genes, reflecting an alteration of acinar identity during ADM (Additional File 8: Fig. S2C-D). Interestingly, Fisher's GSEA also revealed a significant enrichment of genes related to inositol phosphate and phospholipid metabolism and signaling, including *Akt1*, several inositol phosphatases, and several phosphatidylinositol kinases (Fig. 2C,D, Additional File 8: Fig. S2E-F). *Akt1* is an essential node in the PI3K pathway, a well-known player in cell proliferation and oncogenesis, and enrichment of genes related to inositol phosphate signaling further suggest a major role of this pathway, in which a PI3K converts phosphatidylinositol-4, 5-bisphosphate (PIP2) to phosphatidylinositol-3, 4, 5-triphosphate (PIP3) [37]. In pancreatic carcinogenesis, members of the PI3K pathway are not often mutated; however, PI3K signaling is upregulated in human ADM, precursor lesions, and PDAC and can be inhibited to attenuate neoplastic growth [38, 39]. We also observed the enrichment of genes related to Rho, Rac, and Cdc42 GTPase signaling, including many *Arhgef* and *Arhgap* family genes (Fig. 2C,D, Additional File 8: Fig. S2E-F). Rho/Rac/Cdc42 (R/R/C) GTPase pathways act in cytoskeletal organization, which is consistent with morphological cell remodeling observed in ADM. R/R/C GTPases also have known roles in cancer, particularly metastasis, due to their key role in regulating cell

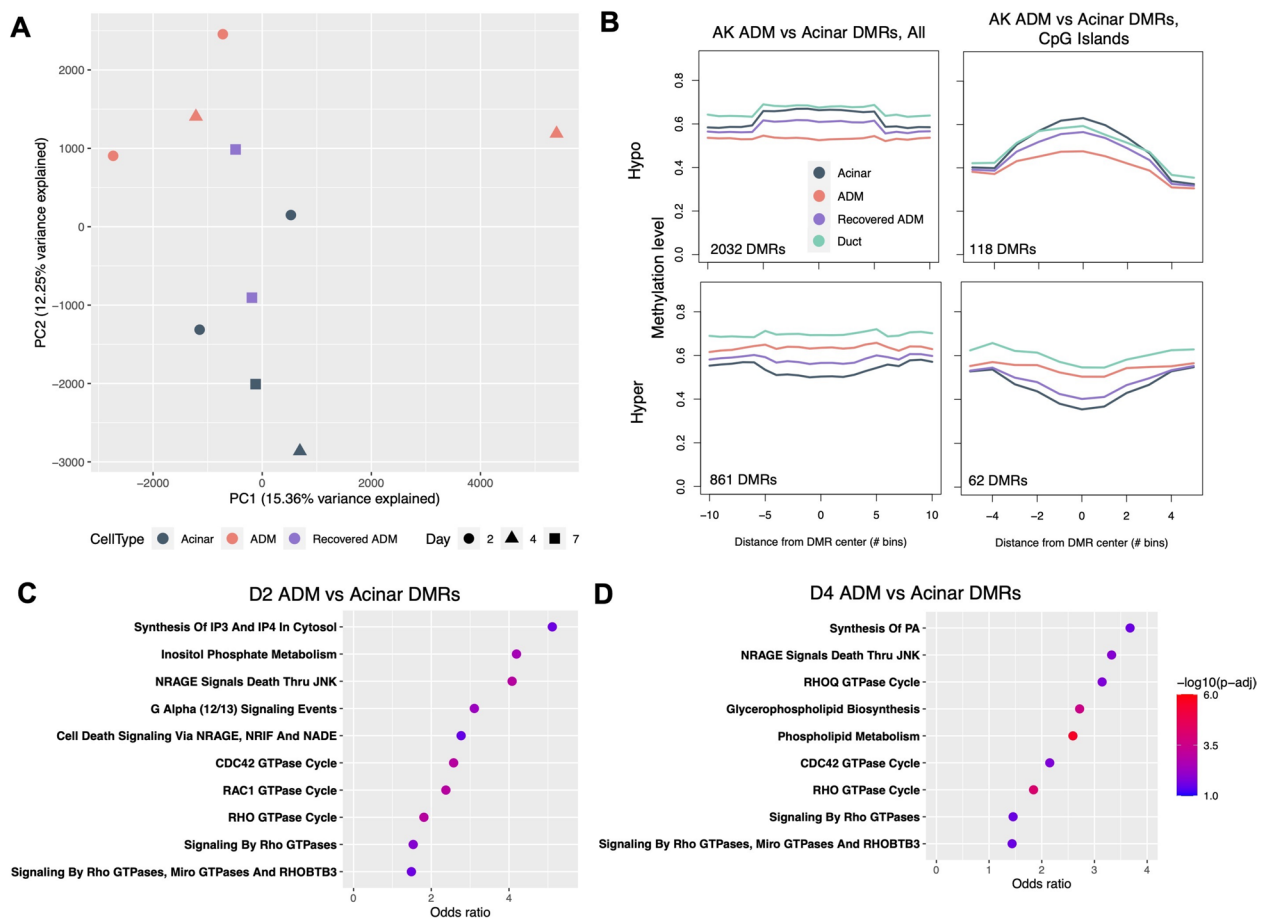


Fig. 2 DNA methylation landscape of exocrine cell types during ADM. **A** Principal component analysis (PCA) of laser capture microdissection-purified acini, ADM lesions, and recovered ADM lesions at PCs 1 and 2. **B** Meta-region plots of AK ADM vs acinar DMRs summarized across all regions (left) and across CpG islands only (right) with 50% width buffer on each side. Methylation levels of recovered ADM lesions and ducts are overlaid. DMR: Differentially methylated region. **C** Fisher's gene set overrepresentation analysis (Fisher's GSEA) of genes overlapping AK model D2 ADM vs acinar DMRs using Reactome 2022 Human gene sets. **D** Fisher's GSEA of genes overlapping AK model D4 ADM vs acinar DMRs using Reactome 2022 Human gene sets. Normal acinar, $n=4$ mice; day 2 ADM, $n=2$ mice; day 4 ADM, $n=2$ mice; day 7 ADM, $n=2$ mice. In B: duct, $n=10$ mice

adhesion and migration [40, 41]. Intriguingly, the PI3K and R/R/C pathways are downstream effectors of *Kras*, the most commonly mutated oncogene in PDAC [42]. We speculated that epigenetic changes during ADM in the *Kras* pathway, whose upregulation is a defining feature of pancreatic cancer, might reflect neoplastic-like activation of *Kras* even without a *Kras* mutation. Thus, we next examined to what extent cells undergoing ADM upregulate gene expression of *Kras*-driven pathways.

DNA methylation changes in *Kras* downstream pathways are associated with gene expression changes

To determine whether the DNA methylation status of *Kras*-regulated pathways was reflected at the transcriptional level, we used 10X Visium spatial transcriptomics (ST) to profile gene expression in the same AK and caerulein pancreata on which LCM and WGBS were

performed (Additional File 6: Table S5) [35]. Importantly, Visium ST allowed us to preserve the tissue architecture of our samples and minimize postmortem autolysis usually exacerbated by single-cell dissociation, while still profiling the samples in a whole-transcriptome manner. Despite the spot-level resolution, rather than single-cell resolution, of 10X Visium ST, the gene expression profiles of ST spots nevertheless generally clustered according to cell type, based on canonical marker gene expression (Fig. 3A, Additional File 9: Fig. S3A-C). To identify broad changes induced by KLF4 overexpression, initial differential gene expression analysis confirmed the recapitulation of ADM-associated signatures in our model. Specifically, 39 genes were upregulated at day 2, including *Muc5ac* and *Tff1*; 836 genes were upregulated in day 4, including *Reg3a*, *Reg3b*, *Reg3g*; and only 10 genes were higher in day 7 versus controls (Additional File 10: Fig. S4A-B).

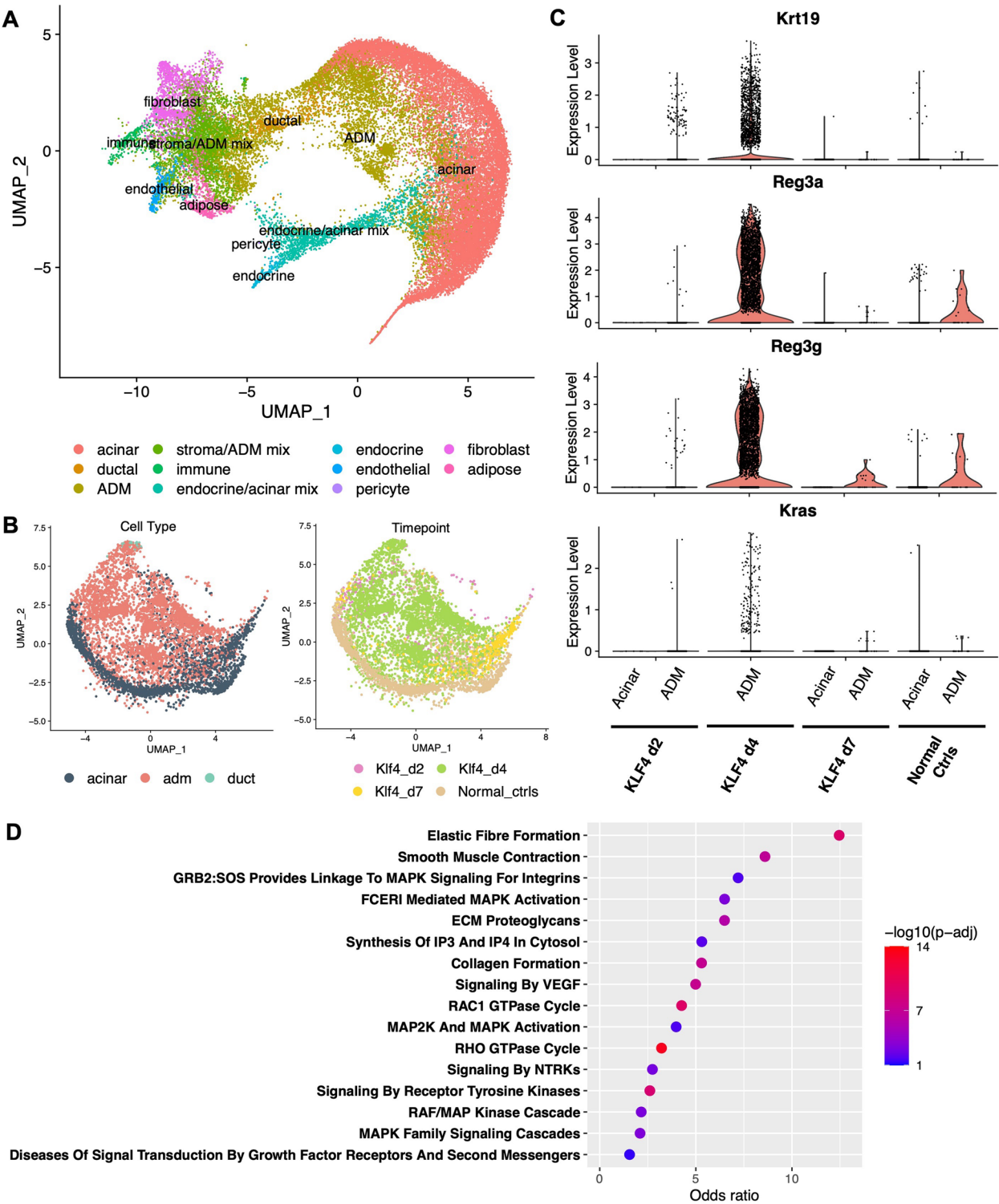


Fig. 3 Gene expression patterns during AK ADM. **A** UMAP projection of all AK mouse Visium ST spots ($n=31,620$ spots). Cell types assigned via canonical marker gene expression. **B** UMAP projection of AK mouse exocrine Visium ST spots only, labeled by cell type (left) and timepoint (right). **C** Relative expression level of canonical ADM marker genes in acinar and/or ADM spots at each timepoint. **D** Selected significantly enriched gene sets from Reactome 2022 Fisher's GSEA performed on the 1412 genes significantly upregulated in highly pure ADM spots relative to highly pure acinar spots. Normal acinar, $n=4$ mice; day 2 ADM, $n=2$ mice; day 4 ADM, $n=2$ mice; day 7 ADM, $n=2$ mice

To estimate the cell type composition of the ST spots, we trained the deconvolution method RCTD [29] using a combination of “pseudo-spot” profiles derived from previously published single-cell data (Additional File 4: Table S4) as well as from profiles of manually annotated histologically pure ST spots from a subset of the ST samples (Methods). Then, we applied RCTD to the remainder of the ST spots to assign cell type proportions to each spot and to identify highly pure exocrine spots (Fig. 3B). We noted that there were fewer ADM spots identified in the D2 sample; however, we attribute this to differences in the severity of the ADM phenotype at each time point and the area of the tissue section profiled by ST at each timepoint. D2 had a less severe histopathology compared to D4 in AK mice, and the tissue sections profiled for D2 were smaller in area than those profiled for D4; therefore, fewer ADM spots at D2 would be expected. The assigned spot identities corresponded well with the known timepoint annotations for each sample (Fig. 3B, Additional File 9: Fig. S3D). Increased expression of canonical ADM markers *Krt19*, *Reg3a*, and *Reg3g* in high-purity ADM spots relative to acinar spots further validated successful deconvolution by RCTD (Fig. 3C).

To examine if differential gene expression in ADM reflected differential methylation, we first compared highly pure ADM spots to highly pure acinar spots and identified more than 1400 significantly differentially expressed genes. Fisher’s GSEA of genes upregulated in ADM spots revealed enrichment of gene sets related to extracellular matrix and collagen formation; receptor tyrosine kinase signaling, including MAPK signaling; and Rho/Rac1 GTPase signaling (Fig. 3D). Examining the expression of specific genes overlapped by AK ADM vs acinar DMRs, many of the same PI3K and R/R/C GTPase pathway genes were indeed upregulated in ADM lesions, including PI3K-related *Akt1*, *Pip4k2b*, and *Ppard*, as well as R/R/C GTPase-related *Arhgef2*, *Gna13*, and *Rock2* (Fig. 4A,B). Fisher’s GSEA of simultaneously differentially methylated and differentially expressed genes confirmed joint enrichment of these pathways (Fig. 4C), demonstrating that pathway-level changes in gene expression during ADM corresponded well with DNA methylation changes. Another known pathway for activation of the Kras

pathway in the absence of Kras mutations is DNA methylation-associated silencing of RAS-effectors including RASSF1A [43] or RASSF5 (NORE1A) [44]. We examined the methylation and gene expression status of these two genes, which were hypomethylated in D4 AK ADM relative to normal acini but were not differentially expressed. Taken together, these data support a model in which ADM cells specifically reprogram the PI3K and R/R/C pathways at both the transcriptional and DNA methylation levels, even in the absence of a Kras mutation.

DNA methylation memory of the ADM transition state

To explore whether signatures of the ADM transition state are preserved even after resolution of ADM, we next asked whether DNA methylation changes seen during ADM were maintained in D7 acini. We identified regions of differential methylation comparing D7 acini to untreated acinar controls in the AK model. Meta-region analysis of all samples revealed that at D7 vs acinar DMRs, D7 acini, on average, had a more extreme methylation level than ADM lesions relative to normal acini, demonstrating that recovered acini did not simply have an intermediate methylation level between peak ADM and normal acini (Fig. 5A).

To verify that these DMRs reflected memory of ADM DMRs at the same pathways, we performed Fisher’s GSEA on genes overlapping D7 vs acinar DMRs (Additional File 11: Table S7). We observed a similar enrichment of PI3K pathway-related gene sets, including synthesis of PIPs at the plasma membrane and phospholipid metabolism (Fig. 5B). These genes included *Pik3cb*, *Tnxb*, and *Depdc5* (Fig. 5C, Additional File 12: Fig. S5A–B). We also determined that D7 vs acinar DMRs overlapped ADM vs acinar DMRs at 326 genes (or 15.7% of the total), indicating that the shared enrichment of PI3K represents methylation memory at many of the same genes (Fig. 5D). To exclude the possibility that the pathway enrichment we had observed in D7 vs acinar DMRs was driven by simply an intermediate methylation level relative to peak ADM during the process of recovery, we repeated Fisher’s GSEA on only DMRs where the D7 methylation level was more extreme than D2 and D4 ADM relative to normal acini. Enrichment of the

(See figure on next page.)

Fig. 4 Integration of differential methylation and expression in AK ADM. Genomic line plots (A) and relative gene expression (B) for selected differentially methylated and differentially expressed PI3K pathway genes (*Akt1*, *Pip4k2b*, *Ppard*) and Rho GTPase family genes (*Arhgef2*, *Gna13*, *Rock2*) in ADM vs acini at each timepoint. In A, tick marks on horizontal axis represent individual CpG sites. In B, KLF4 d4 lacks an acinar violin plot as no spots in these samples were assigned an acinar identity during deconvolution. C Reactome 2022 Fisher’s GSEA enrichment for genes both differentially methylated and differentially expressed in ADM vs acini. Normal acinar, *n* = 4 mice; day 2 ADM, *n* = 2 mice; day 4 ADM, *n* = 2 mice; day 7 ADM, *n* = 2 mice; duct, *n* = 10 mice

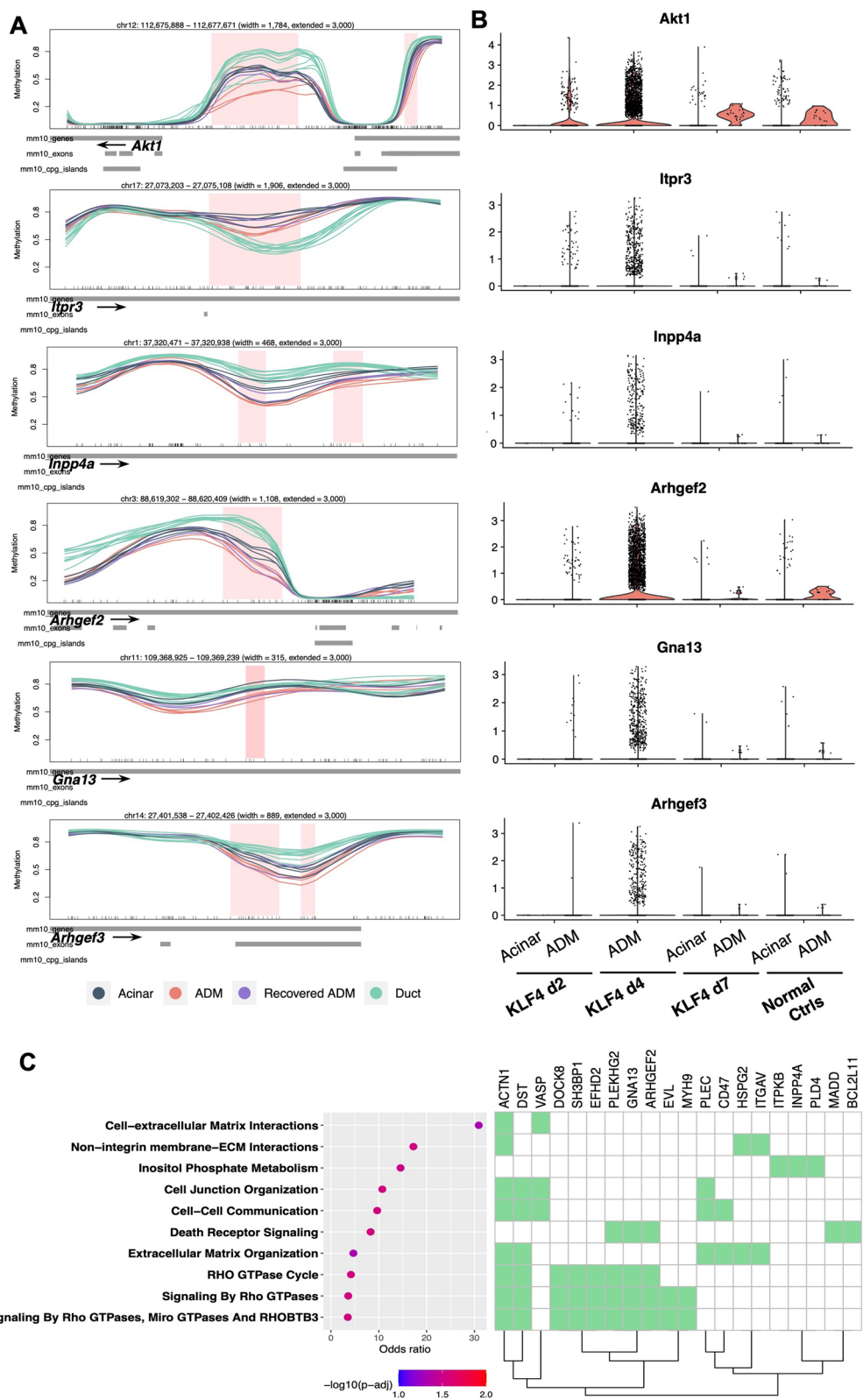


Fig. 4 (See legend on previous page.)

PI3K pathway persisted, driven by genes including *Pten*, *Pik3cb*, and *Sos2* (Additional File 12: Fig. S5C). Although R/R/C GTPase-related genes were not significantly enriched at AK memory DMR genes, we still observed equal or as extreme D7 methylation in several R/R/C-related genes, including *Baiap2l1*, *Dnmbp*, and *Rhoc*, as in ADM (Fig. 5E).

To better assess the timeline of methylation memory and transcriptional resolution, we summarized the methylation and expression of known Reactome- and KEGG-annotated PI3K-related genes at each timepoint. We indeed observed that D7 expression was equivalent to normal control acinar expression, while D7 acini retained differential methylation relative to normal control acini (Fig. 5F). Systematic comparison of methylation and gene expression at known R/R/C-related genes showed a similar but not as drastic pattern (Additional File 12: Fig. S5D). Combined, these results demonstrate that D7 recovered acini retain altered methylation, including at Pi3k pathway genes, even after expression returns to normal.

AP-1, KLF, and pancreatic transcription factor binding is enriched at differentially methylated regions in ADM and in human PanIN lesions

We next investigated what TFs might be acting at ADM vs acinar DMRs to mediate changes in PI3K and R/R/C GTPase activity; thus, we performed TF motif enrichment analysis on these regions. As expected, the KLF4 motif was enriched in the AK D2 ADM vs acinar and D4 ADM vs acinar hypomethylated DMRs, as were those of KLF1 and KLF5, which was unsurprising given their almost identical reverse complementary motifs (Fig. 6A). Interestingly, we also observed an enrichment of AP-1-related motifs, including those of Jun and Fosl2, in D4 ADM vs acinar hypomethylated DMRs (Fig. 6A). Action of AP-1 family TFs including Jun and Fos is consistent with their known role as immediate early genes, or rapid responders to cellular stimuli, including inflammatory stress [45], a characteristic induced by ADM. AP-1 family

TFs also regulate a dynamic balance of cell proliferation and apoptosis and mediate oncogenic transformation, also consistent with processes of morphological and proliferative alterations that occur during ADM [46].

When we investigated DMRs *hypermethylated* in D4 ADM relative to acini, we observed an enrichment of TF motifs related to pancreatic development, including those of Ptf1a, Rbpj, Foxa2, and Gata4 (Fig. 6B), potentially suggesting suppression of target genes that specify acinar identity during ADM. This is consistent with previous studies which suggest that loss of acinar identity promotes neoplasia and that maintenance of acinar identity is sufficient for neoplastic prevention. These prior studies show, for instance, that loss of expression of key acinar TFs Bhlha15 (aka Mist1) or Nr5a2 accelerates pancreatic neoplasia [47, 48], and that sustained Ptf1a overexpression prevents the formation of both precursor and malignant pancreatic lesions and can even revert neoplastic lesions to normal acini [49, 50]. However, further studies will be needed to validate to what extent suppression of these key pancreatic TFs via epigenetic regulation can prevent or reverse neoplasia.

We then asked whether the observed TF enrichments reflected those of neoplastic pancreatic lesions in humans. We used DNA methylation data from available human acinar, ductal, and pancreatic intraepithelial neoplasia (PanIN) samples from our previous study that suggested that PanINs, pancreatic cancer precursor lesions, have an intermediate acinar-ductal DNA methylation signature at the gene level [17]. We examined known human PanIN vs acinar DMRs, again split into PanIN hypo- and hypermethylation. TF motif analysis on DMRs hypomethylated in PanIN lesions remarkably revealed the same enrichment of both AP-1 and KLF family motifs as in DMRs hypomethylated in ADM relative to acini (Fig. 6C, Additional File 13: Table S8). Furthermore, DMRs hypermethylated in PanIN lesions were enriched in motifs of TFs involved in pancreatic development, including NR5A2 and PTF1A, as well as in mesenchymal TFs ZEB1 and SNAI1, which had similar motif sequences to PTF1A (Fig. 6D). To assess

(See figure on next page.)

Fig. 5 DNA methylation memory at PI3K pathway genes following ADM resolution. **A** Meta-region plots of AK day 7 (recovered ADM) vs acinar DMRs summarized across all regions (left) and across CpG islands only (right) with 50% width buffer on each side. **B** Fisher's GSEA of AK day 7 (recovered ADM) vs acinar DMRs using Reactome 2022 Human gene sets. **C** Genomic line plots of DNA methylation at representative PI3K-related genes. **D** Overlap of ADM vs acinar DMRs and day 7 vs acinar DMRs overlapping any gene (left) or overlapping PI3K pathway genes only (right). **E** Genomic line plots of DNA methylation at representative Rho/Rac/Cdc42 GTPase-related genes. **F** Summary heatmap of methylation level and normalized expression level at Reactome- and KEGG-annotated PI3K-related genes for each timepoint. In **C** and **E**, tick marks on horizontal axes represent individual CpG sites



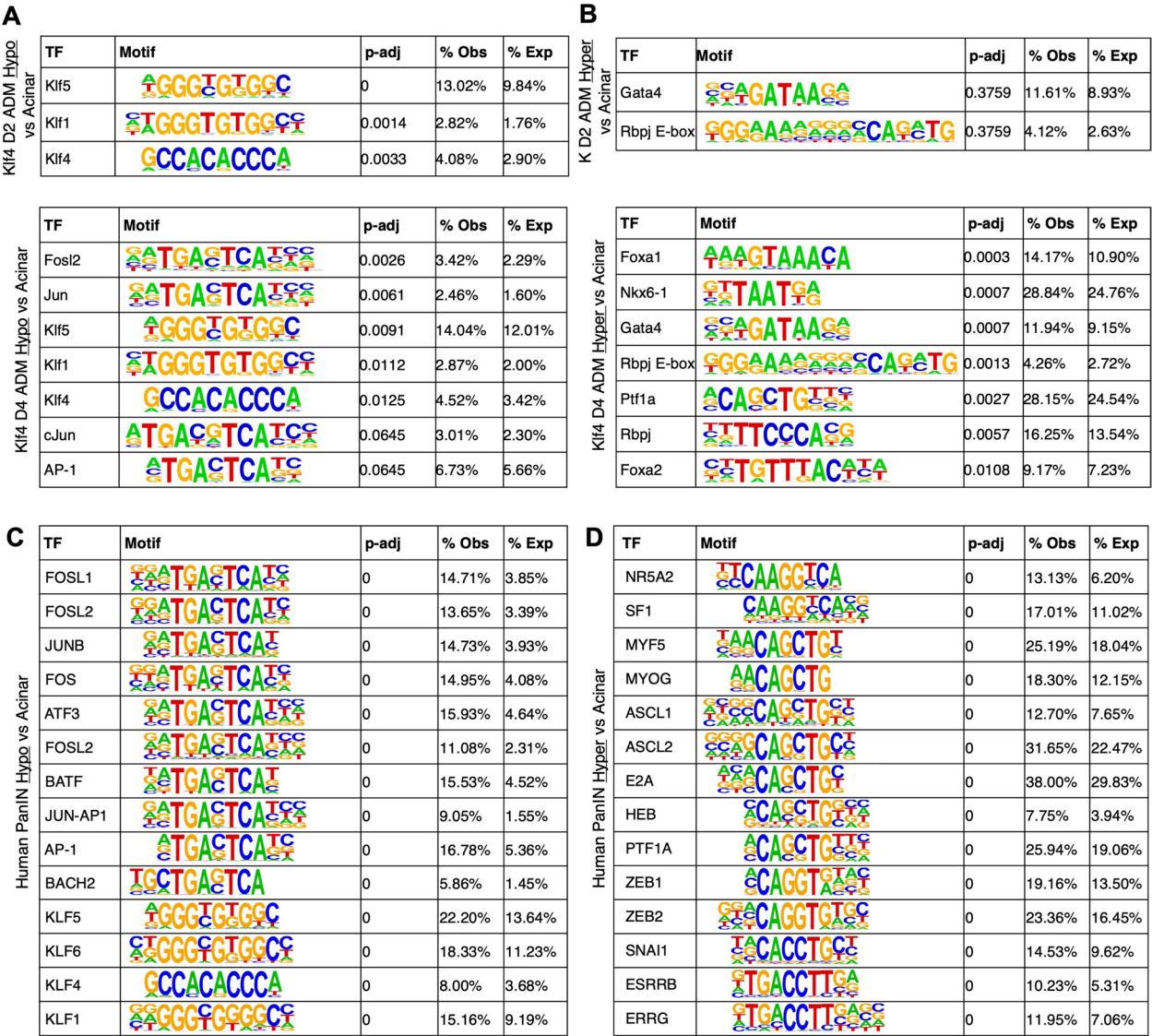


Fig. 6 Consistent transcription factor motif enrichment at mouse ADM and human PanIN DMRs. **A** Motif enrichment analysis results at AK ADM vs acinar hypo DMRs at day 2 (top) and day 4 (bottom). **B** Motif enrichment analysis results at AK ADM vs acinar *hyper* DMRs at day 2 (top) and day 4 (bottom). **A, B**: normal acinar, $n=4$ mice; day 2 ADM, $n=2$ mice; day 4 ADM, $n=2$ mice. Motif enrichment analysis results at human PanIN vs acinar hypo DMRs (**C**) and *hyper* DMRs (**D**). $n=8$ acinar donors, $n=14$ PanIN lesions from 8 donors. p -adj: Adjusted p -values via Benjamini–Hochberg correction

the similarity of mouse and human TF enrichment in a more genome-wide manner, we compared the enrichment of all mouse ADM and human PanIN TF motifs. Generally, TF motifs highly enriched in mouse ADM vs acinar DMRs were also highly enriched in human PanIN vs acinar DMRs, and AP-1 family TFs and pancreatic development TFs were among the most highly enriched for mouse and human hypo- and hyper-methylated DMRs, respectively (Additional File 14: Fig. S6A–B). Taking further advantage of this human data, we

also compared the genes overlapping human PanIN vs acinar DMRs themselves to those overlapping mouse ADM vs acinar DMRs. Fisher’s GSEA on these shared DMR genes identified the Rho GTPase pathway, which included several Arhgap and Cdc42 GTPases in the overlapping set (Additional File 14: Fig. S6C). Together, these results suggest that the signatures and regulatory mechanisms of PanIN development may already be active at the pre-mutant ADM stage and do not require a Kras mutation.

Epigenomic reprogramming of PI3K and R/R/C pathways in caerulein-induced ADM

To help corroborate our findings, we repeated the aforementioned histological and genomic assays using the widely used caerulein model of acute pancreatitis [35]. Although caerulein administration induces ADM, it also has widespread inflammatory digestive effects including increased gastric secretion, gall bladder stimulation, and smooth muscle contraction in the gastrointestinal tract [51], making it difficult to distinguish whether molecular features of ADM result from cell intrinsic activity as opposed to stromal, inflammatory, or systemic physiological influence. Nevertheless, we reasoned that the epigenetic and transcriptional features of ADM would still emerge, even in the presence of non-cell-intrinsic processes. Using the same administration timeline as in the AK model, we similarly observed acinar vacuolation and immune and stromal cell presence at peak pancreatitis on D2, formation of duct-like structures at D4, and resolution to a normal acinar phenotype by D7 (Additional File 15: Fig. S7A), consistent with the morphological features of AK model ADM.

CpG methylation profiles of cell types isolated using laser-capture microdissection (Additional File 6: Table S5), as with AK cell types, grouped by ADM status via PCA (Additional File 15: Fig. S7B-D) even though global methylation levels among acinar-derived cell types did not differ significantly (Additional File 15: Fig. S7E). Combined PCA on ADM lesions, recovered acini, and normal acini from both the AK and caerulein studies clearly separated normal acini from ADM lesions at PCs 2 and 3, with recovered acini again forming an intermediate group (Additional File 15: Fig. S7D). This also supports a biological similarity between the AK and caerulein models of ADM. Examining differential methylation among cell types, the patterns of mean methylation level for ADM vs acinar comparisons in the AK model were less marked but nevertheless held true: at caerulein ADM vs acinar DMRs, D7 recovered samples held an intermediate methylation level between ADM and acinar (Additional File 15: Fig. S7F). At the gene level, Fisher's GSEA of genes overlapping D2 and D4 ADM vs acinar DMRs in the caerulein model further validated the enrichment of genes related to GTPase and inositol phosphate signaling (Additional File 15: Fig. S7G, Additional File 11: Table S7). To corroborate the gene expression signatures observed in the AK model, we also performed 10X Visium ST on caerulein model pancreata (Additional File 6: Table S5), as well as deconvolution with RCTD as before. ST spots clustered according to cell type based on canonical marker gene expression as in the AK model (Additional File 16: Fig. S8A-C).

To evaluate DNA methylation memory in the caerulein model, we again compared D7 recovered acini to normal control acini. We similarly observed that in these DMRs, D7 acini had a more extreme methylation level than ADM lesions did relative to normal control acini (Additional File 17: Fig. S9A). Although there was no significant enrichment of PI3K-related pathways in genes overlapping these DMRs as seen in the AK model, we did observe significant enrichment of R/R/C-related gene sets (Additional File 17: Fig. S9B-C), perhaps suggesting model-specific patterns of DNA methylation memory.

Finally, we performed motif enrichment analysis on caerulein ADM vs acinar DMRs to examine if the same transcriptional regulators would be implicated. We observed the same enrichment of AP-1 family member motifs, including those of *Batf*, *Atf3*, *Jun*, *Fosl1*, and *Fosl2* (Additional File 17: Fig. S9D-F, Additional File 13: Table S8). Interestingly, we did not observe KLF family TFs enriched in DMRs where ADM samples were hypomethylated relative to acinar samples. At DMRs hypermethylated in ADM samples, we again saw motif enrichment of pancreatic development TFs, including *Ptf1a*, *Rbpj*, *Nkx6-1*, *Foxa1*, and *Foxa2*, similarly suggesting a repression of pancreatic identity during ADM (Additional File 17: Fig. S9E-F, Additional File 13: Table S8). Taken together, these results suggest that features of the caerulein model are consistent with a cell-intrinsic induction of ADM.

Single-cell resolution spatial transcriptomics reveals co-expression of multiple cell type signatures in cells undergoing ADM

We next asked if individual cells representing an acinar-ductal transition state could be identified and visualized. We reasoned that single cells with simultaneous expression of acinar, ductal, and even PanIN markers would represent a snapshot of the transition state. Thus, we performed single-cell resolution ST using MERFISH (multiplexed error-robust fluorescence in situ hybridization) on AK D2, D7, and normal control samples (Fig. 7A, Additional File 18: Fig. S10A-B). Our 500-target gene MERFISH panel comprised a mixture of canonical marker genes, differentially methylated genes identified via WGBS, differentially expressed genes identified via 10X Visium ST, and TFs identified via differential motif enrichment analysis (Additional File 3: Table S3). In D2 ADM samples, we indeed identified individual cells simultaneously expressing acinar markers (*Ptf1a*, *Gp2*, *Pnliprp2*), ductal markers (*Krt19*, *Tff1*), and PanIN markers (*Muc5ac*) (Fig. 7A). Interestingly, these cells also expressed PI3K- and AP-1-related genes, including *Akt1*, *Itpr3*, *Pip5k1c*, and *Jund*. Visualization of single cells with co-expression of acinar, ductal, PanIN, PI3K, and AP-1

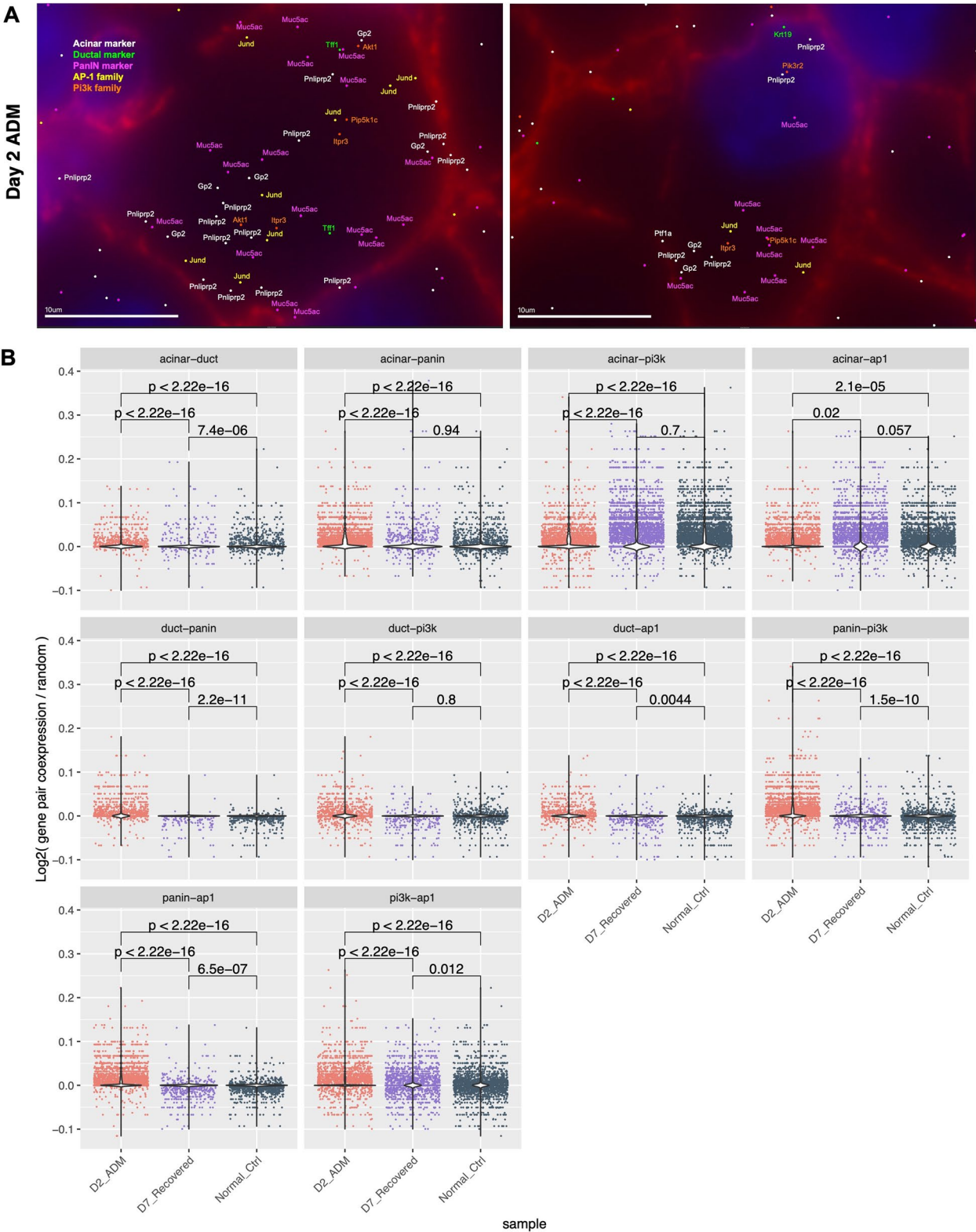


Fig. 7 Joint gene expression signatures at a single-cell resolution. **A** Example ADM cells co-expressing markers of acini (*Pnliprp2*, *Gp2*), ducts (*Tff1*, *Krt19*), panINs (*Muc5ac*), the PI3K pathway (*Akt1*, *Pip5k1c*, *Pik3r2*, *Itp3*), and the AP1 complex (*Jund*). **B** Violin plots of normalized gene pair co-expression proportion in each cell for the two labeled categories. $n = 19,776$ cells. p -values: Wilcoxon rank sum test

marker genes suggests that these cells are actively undergoing an acinar-ductal cell fate transition.

To quantify the abundance of cells in the acinar-ductal transition state among samples in a more systematic manner, we next examined pairwise co-expression of cell type signatures in all cells across all samples (Methods). We found that co-expression of acinar-duct, acinar-PanIN, and PanIN-duct marker gene pairs, normalized by total gene expression, total cell number, and random expectation, occurred most frequently in D2 ADM cells relative to D7 recovered and normal control cells (Fig. 7B), demonstrating increased abundance in D2 ADM of single cells actively in the acinar-ductal transition state. Interestingly, acinar-PI3K pathway co-expression and acinar-AP-1 family co-expression was less abundant in D2 ADM samples than in D7 recovered and normal control cells. We reasoned that this might be due to a decreased abundance of acinar markers in cells undergoing ADM and that ductal and PanIN markers would have more co-expression with PI3K and AP-1 family genes. Indeed, duct-PanIN, duct-PI3K, duct-AP-1, PanIN-PI3K, and PanIN-AP-1 marker co-expression was significantly more abundant in D2 ADM relative to D7 recovered and normal control cells. This further suggests that cells actively in the ADM transition state acquiring more duct-like characteristics also acquire PanIN-like characteristics and upregulate PI3K pathway genes and AP-1-related genes.

Discussion

In this study, we examined epigenetic memory in acinar-ductal metaplasia, we investigated to what extent cells retain DNA methylation memory of the ADM state, and we evaluated the potential upstream regulators and downstream gene expression processes of DNA methylation changes in ADM. We found that during ADM, differential methylation was strongly induced at PI3K and R/R/C GTPase signaling genes, downstream effectors of *Kras*. Consistent with these changes, expression of genes in these pathways was also upregulated during peak ADM. However, differential methylation persisted at these genes following recovery, while gene expression returned to normal, demonstrating that recovered cells retain an epigenetic memory of the transition state at the level of DNA methylation. We implicated AP-1 family transcription factors as positive regulators of ADM, as their motifs were enriched at regions hypomethylated in ADM lesions relative to normal acini. We found that motifs of pancreatic development transcription factors were enriched at regions hypermethylated in ADM lesions. Additionally, we identified and visualized single cells actively in the ADM transition state, which

simultaneously displayed duct- and PanIN-like characteristics and upregulated PI3K- and AP-1-related genes.

While we also used the caerulein model of acute pancreatitis to corroborate our findings, our study can attribute the observed changes in DNA methylation and gene expression to cell-intrinsic expression of KLF4. Finally, our study is highly relevant to human ADM, as the KLF4-induced ADM lesions observed here shared differentially methylated genes with human PanINs, and enrichment of AP-1 motifs and pancreatic development TF motifs was also consistent between mouse ADM and human PanINs. This shared epigenetic signature suggests that ADM lesions acquire characteristics of neoplasia even in the absence of oncogenic mutation. To further evaluate this claim, future studies profiling methylation in mouse models harboring *Kras* mutations, e.g., in the widely used *Kras^{LSL-G12D/+}; Pdx1-Cre* mouse model, will be necessary.

Though ours is the first to identify methylation reprogramming of the PI3K and R/R/C pathways in ADM, previous studies have also examined the behavior of PI3K and R/R/C in pancreatic cancer, although those studies involved oncogenic mutations. PI3K signaling is almost universally activated in murine ADM, PanIN, and PDAC lesions, and inhibition or knockout of PI3K-downstream kinase PDK1 is known to prevent ADM, PanIN, and PDAC formation can be prevented in vivo [38]. Furthermore, the p110 α isoform of PI3K is known to regulate Rho and Rac1 GTPase activity in acinar cells, and inactivation of p110 α inhibits ADM and tumor formation in vivo [39, 52]. There has also been emerging investigation of the relationship of PI3K signaling with cell plasticity. For example, homozygous H1047R gain-of-function mutation in *PIK3CA* has been found to impair the differentiation ability of human induced pluripotent stem cells and to increase their expression of stemness markers [53]. Additionally, human breast cancer samples display an association between increased PI3K signaling level and increased transcriptional cell stemness score [54]. Though further studies will be necessary to evaluate the extent to which the relationship between DNA methylation and transcriptional changes is causal, our study demonstrates DNA methylation-level reprogramming and memory of PI3K and R/R/C pathways in ADM in the absence of oncogenic mutation.

AP-1 also has other known roles in similar models of epithelial inflammation. In skin inflammation, sustained binding of JUN at chromatin domains following an inflammatory stimulus allows rapid re-recruitment of binding partner FOS in response to a secondary stimulus [55]. In mouse models of pancreatic inflammation and pancreatic cancer, AP-1 family motifs are enriched at regions of chromatin that are opened in response to inflammation and that remain open following oncogenic

Kras mutation [7, 56]. These independent findings are consistent with a role of AP-1 family members in epigenetic memory of ADM, though ours is the first to link AP-1 with DNA methylation alterations and memory in ADM. Future studies will help determine the mechanisms by which altered DNA methylation might directly or indirectly affect the behavior of AP-1 family members and pancreatic development TFs. For example, DNA methyltransferases are known to interact directly with AP-1 family members, including JUN, FOS, FOSL1, and FOSL2 in vitro [57], providing a possible recruitment mechanism consistent with differential AP-1 binding at DMRs. Alternatively, TFs are known to preferentially bind motifs based on their methylation status [58, 59], which could also provide specificity to AP-1 and pancreatic TF binding patterns.

As novel methods are developed for performing simultaneous whole-transcriptome and whole-epigenome spatial profiling [60], more will be revealed about the spatial and temporal dynamics of epigenetic memory in inflammation and metaplasia. Although methods for simultaneous transcriptome and DNA methylome profiling currently only exist at the dissociated single cell level [61], already methods have been developed for spatial profiling of the transcriptome and chromatin accessibility simultaneously [62], and for the transcriptome and histone modifications simultaneously [62, 63]. In ADM, co-profiling of the transcriptome and DNA methylome in the same cell will allow precise detection of the point when transcription no longer reflects the methylation pattern of DNA, or in other words, the point when DNA methylation becomes a mark of memory rather than of active regulation.

We speculate that the sustained differential methylation of Kras-downstream pathways even after transcriptional recovery may reflect or even facilitate a selective pressure for sustained Kras activation via an activating oncogenic mutation. We theorize that this could be viewed as a type of oncogene addiction, a well-known characteristic of Kras-mutant cancers including PDAC [64]. Although oncogene addiction is classically viewed as a vulnerability of cancers harboring already-mutated oncogenes, our results could suggest that oncogene “addiction” may begin prior to mutation and may even create a selective pressure for mutation itself. The process of altered DNA methylation preceding oncogene upregulation, addiction, or mutation has precedents [65]. Consistent with this idea, *IDH*-mutant gliomas display DNA hypermethylation at insulator protein CTCF binding sites, resulting in upregulation, although not mutation, of proto-oncogene PDGFRA [66]. On the genome level, it is known that a consequence of global DNA hypomethylation, a known characteristic of most solid tumors [67, 68], is increased

chromosomal instability and therefore increased proto-oncogene and tumor suppressor copy number aberrations [69, 70]. Others have also hypothesized that epigenetic memory of a ductal-like state may be an evolutionary adaptation to more rapidly prevent cell injury in response to secondary inflammatory challenges [7, 55], which would also be consistent with our observations of DNA methylation memory. Further studies will inform the efficacy of potential chemopreventative measures that take advantage of pre-mutant oncogene addiction and epigenetic memory of ADM. The administration of a DNA methylation inhibitor such as azacytidine may be a useful tool for further investigation; however, because the directionality of DMRs between normal acini and ADM lesions is not always the same, unilateral inhibition of DNA methylation with a small molecule drug may not be the best approach for modulating the ADM phenotype. An approach that can specifically demethylate or methylate a targeted region might be a better suited approach for this, or perhaps the administration of Kras pathway inhibitors in at-risk populations prior to oncogenic Kras mutation.

Conclusions

Our study importantly provides a snapshot of the DNA methylome at key points during a cellular transition state associated with cancer initiation and opens the door to understanding underlying processes that may establish and maintain transition states. Our findings of persistent DNA methylation could have applications to cancers generally, especially those in which pre-neoplastic cellular transition states have not already been identified histologically, or might have application to identifying premalignant lesions through liquid biopsy.

Abbreviations

PDAC	Pancreatic ductal adenocarcinoma
ADM	Acinar-to-ductal metaplasia
KLF4	<i>Krüppel-like factor 4</i>
PanIN	Pancreatic intraepithelial neoplasia
AK	<i>Ptf1a-rtTA, TRE-KLF4</i> Mice
H&E	Hematoxylin and eosin
FFPE	Formalin-fixed, paraffin-embedded
LCM	Laser capture microdissection
WGBS	Whole-genome bisulfite sequencing
ST	Spatial transcriptomics
TF	Transcriptional regulator or transcription factor
PCA	Principal component analysis
DMR	Differentially methylated region
R/R/C	<i>Rho/Rac/Cdc42</i>

Supplementary Information

The online version contains supplementary material available at <https://doi.org/10.1186/s13073-025-01452-6>.

Supplementary Material 1

Acknowledgements

We thank Genevieve Stein-O'Brien, Dimitri Sidiropoulos, Zachary Nicholas, and Clare Sengupta for access and training on MERSCOPE. We thank Johns Hopkins Research Animal Resources for assistance with mouse procedures and Johns Hopkins Oncology Tissue Services, Amy Smith, Heather Kulaga, for assistance with tissue and histological procedures. We thank David Tuveson and Ralph Hruban for advice during this work.

Authors' contributions

EKWL, APF, and PC conceived and designed the project. EKWL, AI, and RT acquired the data. EKWL, WZ, WH, HJ, PC, and APF analyzed and interpreted the data. EKWL, PC, and APF drafted and revised the manuscript.

Funding

This work was supported by primarily by NIH Grant CA054358 to APF and NIH Training Grant 5F31CA250489 to EKWL. Some support for supplies was also provided by WH from NIH Grant 1K99HG011468 in lieu of personnel support for APF as a co-mentor with Stephanie Hicks and HJ in her training, and for access to processed data for her own computational algorithm development, which was not used in the present study.

Data Availability

Sequencing data that support the findings of this study are publicly available in Gene Expression Omnibus (GEO) at accession GSE249143 (<https://www.ncbi.nlm.nih.gov/geo/query/acc.cgi?acc=GSE249143>).

Declarations

Ethics approval and consent to participate

All animal procedures were performed in accordance with Johns Hopkins University Animal Care and Use Committee-approved protocols MO18M24 and MO21M20.

Consent to participate not applicable.

Consent for publication

Not applicable.

Competing interests

The authors declare no competing interests.

Author details

¹Department of Biomedical Engineering, Johns Hopkins University School of Medicine, 720 Rutland Avenue, Baltimore, MD 21205, USA. ²Center for Epigenetics, Johns Hopkins University School of Medicine, Baltimore, MD, USA. ³Institute for Cell Engineering, Johns Hopkins University School of Medicine, Baltimore, MD, USA. ⁴Department of Medicine, Johns Hopkins University School of Medicine, 1830 E. Monument Street, Baltimore, MD, USA. ⁵Department of Biostatistics, Johns Hopkins Bloomberg School of Public Health, Baltimore, MD, USA.

Received: 1 October 2024 Accepted: 10 March 2025

Published online: 28 March 2025

References

- Hu J-X, Zhao C-F, Chen W-B, Liu Q-C, Li Q-W, Lin Y-Y, et al. Pancreatic cancer: a review of epidemiology, trend, and risk factors. *World J Gastroenterol*. 2021;27:4298–321.
- Siegel RL, Miller KD, Fuchs HE, Jemal A. Cancer statistics, 2022. *CA: Cancer J Clin*. 2022;72:7–33.
- Storz P. Acinar cell plasticity and development of pancreatic ductal adenocarcinoma. *Nat Rev Gastroenterol Hepatol*. 2017;14:296–304.
- Waddell N, Pajic M, Patch A-M, Chang DK, Kassahn KS, Bailey P, et al. Whole genomes redefine the mutational landscape of pancreatic cancer. *Nature*. 2015;518:495–501.
- Zhang X, Mao T, Zhang B, Xu H, Cui J, Jiao F, et al. Characterization of the genomic landscape in large-scale Chinese patients with pancreatic cancer. *eBioMedicine*. 2022;77:103897.
- Feinberg AP, Levchenko A. Epigenetics as a mediator of plasticity in cancer. *Science*. 2023;379: eaaw3835.
- Poggetto ED, Ho IL, Balestrieri C, Yen EY, Zhang S, Citron F, et al. Epithelial memory of inflammation limits tissue damage while promoting pancreatic tumorigenesis. *Science*. 2021;373: eabj0486.
- Giroux V, Rustgi AK. Metaplasia: tissue injury adaptation and a precursor to the dysplasia–cancer sequence. *Nat Rev Cancer*. 2017;17:594–604.
- Feinberg AP. The key role of epigenetics in human disease prevention and mitigation. Longo DL, editor. *N Engl J Med*. 2018;378:1323–34.
- Kim M, Costello J. DNA methylation: an epigenetic mark of cellular memory. *Exp Mol Med*. 2017;49: e322–e322.
- Kim K, Zhao R, Doi A, Ng K, Unternaehrer J, Cahan P, et al. Donor cell type can influence the epigenome and differentiation potential of human induced pluripotent stem cells. *Nat Biotechnol*. 2011;29:1117–9.
- Han DW, Tapia N, Hermann A, Hemmer K, Höing S, Araújo-Bravo MJ, et al. Direct reprogramming of fibroblasts into neural stem cells by defined factors. *Cell Stem Cell*. 2012;10:465–72.
- McDonald OG, Li X, Saunders T, Tryggvadottir R, Mentch SJ, Warmoes MO, et al. Epigenomic reprogramming during pancreatic cancer progression links anabolic glucose metabolism to distant metastasis. *Nat Genet*. 2017;49:367–76.
- Makohon-Moore AP, Zhang M, Reiter JG, Bozic I, Allen B, Kundu D, et al. Limited heterogeneity of known driver gene mutations among the metastases of individual patients with pancreatic cancer. *Nat Genet*. 2017;49:358–66.
- Roe J-S, Hwang C-I, Somerville TDD, Milazzo JP, Lee EJ, Da Silva B, et al. Enhancer reprogramming promotes pancreatic cancer metastasis. *Cell*. 2017;170:875–888.e20.
- Fitz-James MH, Cavalli G. Molecular mechanisms of transgenerational epigenetic inheritance. *Nat Rev Genet*. 2022;23:325–41.
- Lo EKW, Mears BM, Maurer HC, Idrizi A, Hansen KD, Thompson ED, et al. Comprehensive DNA methylation analysis indicates that pancreatic intraepithelial neoplasia lesions are acinar-derived and epigenetically primed for carcinogenesis. *Cancer Res*. 2023;83:1905–16.
- Nunn A, Otto C, Fasold M, Stadler PF, Langenberger D. Manipulating base quality scores enables variant calling from bisulfite sequencing alignments using conventional bayesian approaches. *BMC Genomics*. 2022;23:477.
- Garrison E, Marth G. Haplotype-based variant detection from short-read sequencing. *arXiv*; 2012:1207.3907.
- Hu H, Ye Z, Qin Y, Xu X, Yu X, Zhuo Q, et al. Mutations in key driver genes of pancreatic cancer: molecularly targeted therapies and other clinical implications. *Acta Pharmacol Sin*. 2021;42:1725–41.
- Mayakonda A, Lin D-C, Assenov Y, Plass C, Koeffler HP. Maftools: efficient and comprehensive analysis of somatic variants in cancer. *Genome Res*. 2018;28:1747–56.
- Krueger F, Andrews SR. Bismark: a flexible aligner and methylation caller for Bisulfite-Seq applications. *Bioinformatics*. 2011;27:1571–2.
- Hansen KD, Langmead B, Irizarry RA. BSmooth: from whole genome bisulfite sequencing reads to differentially methylated regions. *Genome Biol*. 2012;13: R83.
- Xie Z, Bailey A, Kuleshov MV, Clarke DJB, Evangelista JE, Jenkins SL, et al. Gene set knowledge discovery with enrichr. *Current Protocols*. 2021;1: e90.
- Cavalcante RG, Sartor MA. annotatr: genomic regions in context. *Bioinformatics*. 2017;33:2381–3.
- Lawrence M, Huber W, Pagès H, Aboyoun P, Carlson M, Gentleman R, et al. Software for computing and annotating genomic ranges. *PLoS Comput Biol*. 2013;9: e1003118.
- Wickham H. ggplot2: elegant graphics for data analysis. 1st ed. Springer; 2009.
- Hao Y, Hao S, Andersen-Nissen E, Mauck WM, Zheng S, Butler A, et al. Integrated analysis of multimodal single-cell data. *Cell*. 2021;184:3573–3587.e29.
- Cable DM, Murray E, Zou LS, Goeva A, Macosko EZ, Chen F, et al. Robust decomposition of cell type mixtures in spatial transcriptomics. *Nat Biotechnol*. 2022;40:517–26.
- Subramanian A, Tamayo P, Mootha VK, Mukherjee S, Ebert BL, Gillette MA, et al. Gene set enrichment analysis: a knowledge-based approach for interpreting genome-wide expression profiles. *Proc Natl Acad Sci*. 2005;102:15545–50.

31. Heinz S, Benner C, Spann N, Bertolino E, Lin YC, Laslo P, et al. Simple combinations of lineage-determining transcription factors prime cis-regulatory elements required for macrophage and B cell identities. *Mol Cell*. 2010;38:576–89.
32. Liao X, Sharma N, Kapadia F, Zhou G, Lu Y, Hong H, et al. Krüppel-like factor 4 regulates macrophage polarization. *J Clin Invest*. 2011;121:2736–49.
33. Talmasov D, Zhang X, Yu B, Nandan MO, Bialkowska AB, Elkarim E, et al. Krüppel-like factor 4 is a radioprotective factor for the intestine following γ -radiation-induced gut injury in mice. *Am J Physiol-Gastrointest Liver Physiol*. 2015;308:G121–38.
34. Wei D, Wang L, Yan Y, Jia Z, Gagea M, Li Z, et al. KLF4 is essential for induction of cellular identity change and acinar-to-ductal reprogramming during early pancreatic carcinogenesis. *Cancer Cell*. 2016;29:324–38.
35. Lo EKW, Idrizi A, Tryggvadottir R, Zhou W, Hou W, Ji H, et al. DNA methylation memory of acinar-ductal transition state altering Kras-downstream PI3K and Rho GTPase signaling. *Gene Expression Omnibus; GSE249143*.
36. Irizarry RA, Ladd-Acosta C, Wen B, Wu Z, Montano C, Onyango P, et al. The human colon cancer methylome shows similar hypo- and hypermethylation at conserved tissue-specific CpG island shores. *Nat Genet*. 2009;41:178–86.
37. Hoxhaj G, Manning BD. The PI3K–AKT network at the interface of oncogenic signalling and cancer metabolism. *Nat Rev Cancer*. 2020;20:74–88.
38. Eser S, Reiff N, Messer M, Seidler B, Gottschalk K, Dobler M, et al. Selective requirement of PI3K/PDK1 signaling for Kras oncogene-driven pancreatic cell plasticity and cancer. *Cancer Cell*. 2013;23:406–20.
39. Wu CYC, Carpenter ES, Takeuchi KK, Halbrook CJ, Peverley LV, Bien H, et al. PI3K regulation of Rac1 Is Required for KRAS-Induced Pancreatic Tumorigenesis in Mice. *Gastroenterology*. 2014;147:1405–1416.e7.
40. Crosas-Mollet E, Samain R, Kohlhammer L, Orgaz JL, George SL, Maiques O, et al. Rho GTPase signaling in cancer progression and dissemination. *Physiol Rev*. 2022;102:455–510.
41. Maldonado M del M, Medina JI, Velazquez L, Dharmawardhane S. Targeting Rac and Cdc42 GEFs in Metastatic Cancer. *Front Cell Dev Biol*. 2020;8:201.
42. Roman M, Hwang E, Sweet-Cordero EA. Synthetic Vulnerabilities in the KRAS Pathway. *Cancers*. 2022;14: 2837.
43. Dammann R, Li C, Yoon J-H, Chin PL, Bates S, Pfeifer GP. Epigenetic inactivation of a RAS association domain family protein from the lung tumour suppressor locus 3p21.3. *Nat Genet*. 2000;25:315–9.
44. Irimia M, Fraga MF, Sanchez-Céspedes M, Esteller M. CpG island promoter hypermethylation of the Ras-effector gene NORE1A occurs in the context of a wild-type K-ras in lung cancer. *Oncogene*. 2004;23:8695–9.
45. Hess J, Angel P, Schorpp-Kistner M. AP-1 subunits: quarrel and harmony among siblings. *J Cell Sci*. 2004;117:5965–73.
46. Shaulian E, Karin M. AP-1 as a regulator of cell life and death. *Nat Cell Biol*. 2002;4:E131–6.
47. Shi G, Zhu L, Sun Y, Bettencourt R, Damsz B, Hruban RH, et al. Loss of the Acinar-Restricted Transcription Factor Mist1 Accelerates Kras-Induced Pancreatic Intraepithelial Neoplasia. *Gastroenterology*. 2009;136:1368–78.
48. von Figura G, Morris JP, Wright CVE, Hebrok M. Nr5a2 maintains acinar cell differentiation and constrains oncogenic Kras-mediated pancreatic neoplastic initiation. *Gut*. 2014;63:656–64.
49. Krah NM, De La OJP, Swift GH, Hoang CQ, Willet SG, Chen Pan F, et al. The acinar differentiation determinant PTF1A inhibits initiation of pancreatic ductal adenocarcinoma. *Green MR, editor eLife*. 2015;4:e07125.
50. Krah NM, Narayanan SM, Yugawa DE, Straley JA, Wright CVE, MacDonald RJ, et al. Prevention and Reversion of Pancreatic Tumorigenesis through a Differentiation-Based Mechanism. *Dev Cell*. 2019;50:744–754.e4.
51. Bertaccini G, De Caro G, Endean R, Rspamer V, Impicciatore M. The actions of caerulein on the smooth muscle of the gastrointestinal tract and the gall bladder. *Br J Pharmacol*. 1968;34:291–310.
52. Baer R, Cintas C, Dufresne M, Cassant-Sourdy S, Schönhuber N, Planque L, et al. Pancreatic cell plasticity and cancer initiation induced by oncogenic Kras is completely dependent on wild-type PI 3-kinase p110 α . *Genes Dev*. 2014;28:2621–35.
53. Madsen RR, Knox RG, Pearce W, Lopez S, Mahler-Araujo B, McGranahan N, et al. Oncogenic PIK3CA promotes cellular stemness in an allele dose-dependent manner. *Proc Natl Acad Sci*. 2019;116:8380–9.
54. Madsen RR, Erickson EC, Rueda OM, Robin X, Caldas C, Toker A, et al. Positive correlation between transcriptomic stemness and PI3K/AKT/mTOR signaling scores in breast cancer, and a counterintuitive relationship with PIK3CA genotype. *PLoS Genet*. 2021;17: e1009876.
55. Larsen SB, Cowley CJ, Sajjath SM, Barrows D, Yang Y, Carroll TS, et al. Establishment, maintenance, and recall of inflammatory memory. *Cell Stem Cell*. 2021;28:1758–1774.e8.
56. Li Y, He Y, Peng J, Su Z, Li Z, Zhang B, et al. Mutant Kras co-opts a proto-oncogenic enhancer network in inflammation-induced metaplastic progenitor cells to initiate pancreatic cancer. *Nat Cancer*. 2021;2:49–65.
57. Hervouet E, Peixoto P, Delage-Mourroux R, Boyer-Guittaut M, Cartron P-F. Specific or not specific recruitment of DNMTs for DNA methylation, an epigenetic dilemma. *Clin Epigenetics*. 2018;10:17.
58. Yin Y, Morgunova E, Jolma A, Kaasinen E, Sahu B, Khund-Sayeed S, et al. Impact of cytosine methylation on DNA binding specificities of human transcription factors. *Science*. 2017;356: eaaj2239.
59. Fang Y, Ji Z, Zhou W, Abante J, Koldobskiy MA, Ji H, et al. DNA methylation entropy is associated with DNA sequence features and developmental epigenetic divergence. *Nucleic Acids Res*. 2023;51:2046–65.
60. Casado-Pelaez M, Bueno-Costa A, Esteller M. Single cell cancer epigenetics. *Trends in Cancer*. 2022;8:820–38.
61. Hu Y, Huang K, An Q, Du G, Hu G, Xue J, et al. Simultaneous profiling of transcriptome and DNA methylome from a single cell. *Genome Biol*. 2016;17:88.
62. Zhang D, Deng Y, Kukanja P, Agirre E, Bartosovic M, Dong M, et al. Spatial epigenome–transcriptome co-profiling of mammalian tissues. *Nature*. 2023;616:113–22.
63. Lu T, Ang CE, Zhuang X. Spatially resolved epigenomic profiling of single cells in complex tissues. *Cell*. 2022;185:4448–4464.e17.
64. Luo J. KRAS mutation in pancreatic cancer. *Semin Oncol*. 2021;48:10–8.
65. Wajed SA, Laird PW, DeMeester TR. DNA methylation: an alternative pathway to cancer. *Ann Surg*. 2001;234:10.
66. Flavahan WA, Drier Y, Liao BB, Gillespie SM, Venteicher AS, Stemmer-Rachamimov AO, et al. Insulator dysfunction and oncogene activation in IDH mutant gliomas. *Nature*. 2016;529:110–4.
67. Timp W, Bravo HC, McDonald OG, Goggins M, Umbricht C, Zeiger M, et al. Large hypomethylated blocks as a universal defining epigenetic alteration in human solid tumors. *Genome Med*. 2014;6:61.
68. Feinberg AP, Vogelstein B. Hypomethylation distinguishes genes of some human cancers from their normal counterparts. *Nature*. 1983;301:89–92.
69. Chen RZ, Pettersson U, Beard C, Jackson-Grusby L, Jaenisch R. DNA hypomethylation leads to elevated mutation rates. *Nature*. 1998;395:89–93.
70. Besseling N, Keijer J, Vermeulen C, Boymans S, de Ridder J, van Hoeck A, et al. The genome-wide mutational consequences of DNA hypomethylation. *Sci Rep*. 2023;13:6874.

Publisher's Note

Springer Nature remains neutral with regard to jurisdictional claims in published maps and institutional affiliations.